Engineering Fracture Mechanics 301 (2024) 110028

Contents lists available at ScienceDirect

Engineering Fracture Mechanics

journal homepage: www.elsevier.com/locate/engfracmech

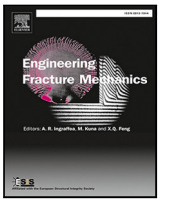

Characterisation of mode-I fracture resistance of adhesive layers with imperfections

Leo Škec [a], Giulio Alfano [b,*]

[a] Faculty of Civil Engineering, University of Rijeka, Radmile Matejčić 3, 51000 Rijeka, Croatia
[b] Department of Mechanical and Aerospace Engineering, Brunel University London, Kingston Lane, Uxbridge UB8 3PH, UK

ARTICLE INFO

Keywords:
Adhesive joints
Mode-I delamination
DCB experiment
Fracture resistance
Cohesive-zone models

ABSTRACT

In this work, a novel procedure to evaluate the influence of imperfections at the interface (such as voids and interfacial failure) on the fracture resistance of adhesive joints in mode-I debonding is proposed, based on an image-processing analysis of the crack surface. Its application to the characterisation of fracture resistance of aluminium DCB specimens bonded with an epoxy adhesive leads to a more accurate evaluation of the 'effective' fracture resistance by taking into account the distribution of imperfections along the interface, therefore also confirming that the typical oscillations and drops in the load–displacement curve can be attributed to the imperfections.

1. Introduction

Adhesives are nowadays applied to join structural components in a variety of industries, such as automotive, aerospace and civil engineering. Thus, a proper design of adhesively bonded structures must also include an assessment of their resistance to failure. The most common and critical failure mode of adhesive joints, in which the adhesive connection between two (or more) structural components is lost, is known as debonding or delamination. In order to assess the resistance of an adhesive to debonding, it is necessary to perform tailored experiments on adhesive joints, from which relevant material parameters of the adhesive can be determined for design purposes.

In this work, the attention will be focused on mode-I (normal) debonding and, in particular, on some challenges posed by the presence of defects within the adhesively bonded interface and how to address them to obtain a more accurate evaluation of the fracture resistance. Defects on the interface, such as voids or areas of poor adhesion (including interfacial failure), can significantly decrease the bearing capacity of the adhesive joint locally and, in turn, alter the computed values of the fracture resistance. Sometimes they may also lead to unstable crack propagation on part of the crack path.

Nucleation of voids in adhesive layers and their effects on structural behaviour of adhesive joints have been studied by several authors in the last 50 years. Possible causes investigated include trapped air within the adhesive [1,2], moisture absorption [3,4], substrate surface treatment [2,3], pressure applied during curing [3], remaining solvent or water from manufacture [4], adhesive shrinkage [5]. The effects include reduction in durability and in T-peel and honeycomb peel strengths [4] and could depend on the adhesive thickness according to Lißner et al. [6] who noticed that the thinner the adhesive, the larger the volume fraction of voids. By using edited photographs of the fracture surfaces, Smith [7] created an overlay of the upper and lower adhesive regions in order to identify the failure mechanism (cohesive or interfacial) at the interface of DCB specimens, determine the percentage of interface

* Corresponding author.
E-mail address: giulio.alfano@brunel.ac.uk (G. Alfano).

https://doi.org/10.1016/j.engfracmech.2024.110028
Received 10 October 2023; Received in revised form 19 February 2024; Accepted 19 March 2024
Available online 6 April 2024

Nomenclature

α	Fraction of the contribution of the interfacial-failure fracture resistance with respect to the cohesive-failure fracture resistance
α^*	Ratio between the shear and bending stiffness of a single DCB arm
Δa^E	Difference between the actual crack length a and the equivalent crack length a_{eq}^E
Δv	Increment of the cross-head displacement
$\hat{G}_c^{eff}$	Average value of the effective critical energy release rate
μ	Shear modulus of the bulk material
ν	Poisson's ratio of the bulk material
Ω	Work of separation (the area under the TSL)
$\overline{\zeta}_m$	Average value of ζ_m
$\overline{G}_c^{app}$	Average value of G_c^{app}
$\overline{G}_{c.i}^{app}$	Average value of G_c^{app} determined at point i
Π	Total potential energy
σ_{max}	Peak interface traction in the bi-linear TSL
ζ	Defect-distribution coefficient
ζ_b	Defect-distribution coefficient on the bottom face
ζ_m	Mean value of the defect-distribution coefficient
ζ_t	Defect-distribution coefficient on the top face
$\zeta_{m.i}$	Mean value of the defect-distribution coefficient determined at point i
A	Cross-sectional area of a single DCB arm
a	Crack length
a_0	Initial crack length
A_s	Shear-corrected cross-sectional area of a single DCB arm
a_{eq}	Equivalent crack length based on Timoshenko beam theory according to ESBT
a_{eq}^E	Equivalent crack length based on Euler–Bernoulli beam theory
a_{max}	Maximal value of the crack length
b	Width of a DCB specimen
b_i	Total area of interfacial failure on both plates per unit of length
b_{db}	Area of defects per unit of length on the bottom face
b_{dt}	Area of defects per unit of length on the top face
b_{dv}	Area of voids per unit of length
b_{eff}	Effective width of the adhesive layer
b_{ib}	Area of interfacial failure per unit of length on the bottom face
b_{it}	area of interfacial failure per unit of length on the top face
c	Height of the loading block for a DCB specimen
d	Thickness of a single DCB arm
E	Young's modulus of the bulk material
F	Applied load
F_{max}	Maximal value of the applied load
G_c	Critical energy release rate
G_c^{app}	Apparent critical energy release rate
G_c^{eff}	Effective critical energy release rate
G_c^E	Critical energy release rate based on Euler–Bernoulli beam theory
I	Cross-sectional second moment of area for each DCB arm
i	Counter for the points along the interface in which $\zeta_{m.i}$ and $\overline{G}_{c.i}^{app}$ are determined
k	Stiffness of the linear-elastic part of the bi-linear TSL

defects and correlate them to the measured fracture resistance using nonlinear regression, but without incorporating the defects in a numerical model of the DCBs.

Patterned interfaces, in which regular patterns of voids or weak areas are intentionally introduced in the bondline, can be used to investigate the influence of heterogeneities (imperfections) at the interface on the stability of crack propagation and on the fracture resistance of joints [8–10].

k_s	Shear-correction coefficient
L	Length of a DCB specimen
n	Total number of points along the interface in which $\zeta_{m.i}$ and $\overline{G}_{c.i}^{app}$ are determined
t	Bondline thickness
v	Cross-head displacement of a DCB specimen
x	Co-ordinate along the direction of crack propagation
DCB	Double Cantilever Beam
DPZ	Damage-Process Zone
ESBT	Enhanced Simple Beam Theory
SEM	Scanning Electron Microscope
TSL	Traction-Separation Law

In particular, Heide-Jørgensen and Budzik [10,11] performed DCB experiments on joints with patterned interfaces [10] or with a single interface discontinuity [11] and developed an analytical model that can successfully describe a sudden drop of force, i.e. reduction in the joint's load carrying capacity as the crack approaches the void. When the size of voids is much smaller than the process-zone size, the force–displacement curve is smooth and resembles a stable crack growth, while for larger voids, an oscillating behaviour related to the crack crossing sharp transitions, i.e. strong/weak adhesion zones, can be noticed. They correctly recognised that the effective fracture energy in that case can be misinterpreted as a property of the 'bulk' (without the 'voids') bondline. Thus, they concluded that if the properties of a perfect/homogeneous material are known in advance, the difference between the 'measured' and 'perfect' properties could be related to size and distribution of voids inside the bondline.

Budzik et al. [12] also investigated mode-I fracture behaviour of width-varying DCB specimens (arms), but with such specimens it is not possible to isolate the influence of the changing adhesive width on the load-bearing capacity of the adhesive joint as the width of the arms also changes simultaneously. Moreover, the specimens studied by Budzik et al. in Ref. [12] had a regular change of width (defined by a function) along the specimen.

Although the last cited articles (Refs. [7–12]) shed some light on the effect of defects, a systematic procedure to detect the presence and extract the distribution of interface defects on broken specimens and a rigorous quantitative evaluation of their effects on the structural response have not yet been provided and are the main research gaps addressed in this article. To this end, a post-mortem analysis of broken DCB specimens, previously tested by the present authors (see Ref. [13]), is presented. It reveals a non-negligible part of the interface characterised by either patches of interfacial failure or by the presence of voids within the adhesive. In fact, the aim of the work presented in this article is not to investigate the reasons why defects can be present on the interface, but rather to study the relation between these defects and the characteristic bumps in the load–displacement curves that are found by many authors testing similar types of adhesives, which also result in oscillating R-curves [14–17]. A second aim is to propose a multi-parameter material model that could take these effects into account, so that a more accurate determination of the fracture resistance of the adhesive is obtained.

To achieve the above aim, a novel method is presented, which is based on some simple-to-implement image processing followed by a procedure developed to extract the distribution and nature of defects so that these can be translated in a reduction of the effective width of the adhesive due to voids/interfacial failure. A multi-parameter material model that takes these effects into account is then used, so that a more accurate determination of the fracture resistance of the adhesive is obtained.

By taking into account the defects at the interface, it is possible to compute what we will indicate in this paper as the 'effective' value of G_c and denote by G_c^{eff}. Instead, by not accounting for the reduced amount of adhesive, the value of G_c is lower than the effective one and we will indicate it as 'apparent' and denote it by G_c^{app}. More generally, in this paper we will use the adjectives 'effective' or 'apparent' next to a parameter or property to imply that the parameter or property takes into account or not the presence of imperfections, respectively.

Some interplay between the defects of the interface and its rate dependence can take place [11]. However, as stated by Blackman et al. [18], the effects of material rate dependence could be negligible under quasi-static conditions and are not expected unless the strain rate varies across few orders of magnitude. Therefore, also with a view to focussing on the original aspects of this present contribution, in this paper rate dependence will not be specifically considered and the focus will be on the experiments conducted at a single speed, namely at 0.1 mm/min.

2. Experimental tests and results

Experimental tests have been carried out on DCB specimens made of aluminium Al 6082-T6 bonded with Araldite® 2015 structural adhesive. The preparation of the specimens was done according to BS ISO 25217:2009 [19] and the technical data sheet provided by the manufacturer [20]. The average value of the adhesive thickness for the 4 considered specimens was 0.15 mm with a coefficient of variation equal to 17%, which is less than the limit value reported in the standard (20%). Geometrical properties of the specimens are reported in Fig. 1 and Table 1. Young's modulus and Poisson's ratio of the aluminium read $E = 70700$ MPa and $\nu = 1/3$. Loading blocks were used to attach the specimens to the tensile testing machine. Four debonding tests have been performed

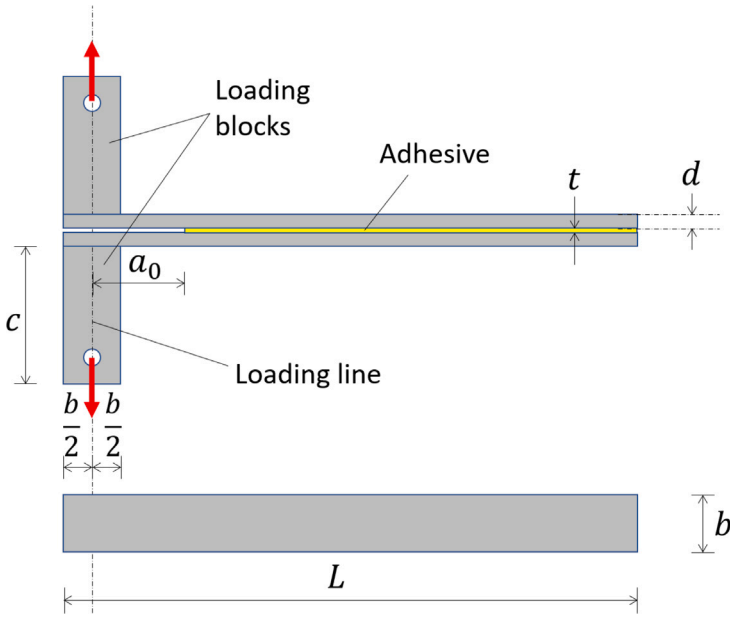

Fig. 1. Geometry of DCBs tested; dimensions are reported in Table 1.

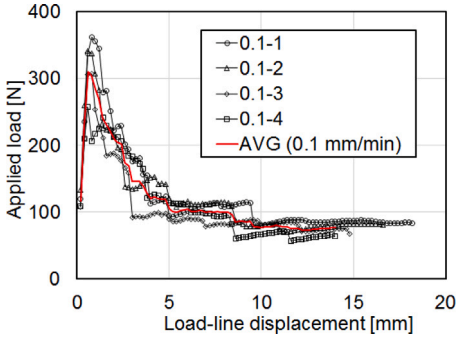

Fig. 2. Experimental individual load–displacement curves for the 4 tested specimens and the corresponding average curve.

Table 1
Dimensions of the DCB specimens according to Fig. 1.

Dimensions [mm]	L	d	b	a_0	c	t
Average value	250	6.35	25.4	40	60	0.15

at cross-head displacement speed of 0.1 mm/min. The tests were performed at room temperature using a 30 kN electromechanical Instron testing machine. More details about the experimental set up can be found in [13].

The individual load–displacement curves for 4 tests together with the corresponding average are given in Fig. 2. Notice that, in order to produce a single average curve, the raw data from the test were postprocessed and an average computed for each cross-head displacement increment of 0.2 mm. This is why load–displacement data for values of the cross-head displacement less than 0.2 mm is not given in the plot. As shown in [13], such load–displacement data result in R-curves where similar experimental scatter can be noticed.

As reported in [13] and shown in Fig. 3 for a representative specimen, post-mortem analysis of the broken specimens revealed several defects in the adhesive layer. These are either areas where interfacial failure has occurred, or areas with complete lack of adhesion, which we will refer to as 'voids' for simplicity. Although investigating the causes for these imperfections is outside the scope of this paper, the following observations can be made. Voids can be created if the adhesive layers on two adjacent plates do not completely connect after pressing the plates together due to insufficient thickness of the adhesive or trapped air. On the other hand, it is also possible that curing of the adhesive generates the voids due to shrinkage of the material.

After analysing the crack surfaces of all tests, it can be concluded that the voids are more frequent and larger than the interfacial-failure zones. The only explanation for occasional interfacial failure could be some grease or dirt that remained on the

surface after cleaning, although such problems have not been noticed during the preparation of the specimens. As explained in the introduction, voids and/or interfacial failure in the adhesive layer must have an influence on the computed fracture resistance, which is investigated in detail in the following section.

3. Evaluation of the effective fracture resistance by accounting for interface defects

In the following subsections, the difference between the effective and apparent fracture resistance will be defined depending on whether the defects on the interface are taken into account or not.

3.1. Apparent vs. effective fracture resistance

As discussed in the previous section, there are two principal types of defects at the interface, namely (a) interfacial failure and (b) voids. In general, it is reasonable to assume that both of them reduce the fracture resistance and therefore cause local bumps in the load–displacement curves. In fact, by assuming that the DCB arms act as Euler–Bernoulli beams clamped at the crack tip, the critical energy release rate can be approximated as [21]

$$G_c \approx G_c^E = \frac{1}{b}\sqrt[3]{\frac{9F^4 v^2}{4EI}} \tag{1}$$

where superscript E refers to Euler–Bernoulli beam theory, F is the applied load, v is the cross-head displacement and EI is the bending stiffness of a single DCB arm. From Eq. (1), it follows that a reduction in the fracture resistance G_c leads to a drop of the force F for the same values of the remaining parameters. As shown in [21], formula (1) for G_c^E, in which only the measured force–displacement data is required, gives a very accurate approximation of both G_c and the work of separation Ω (area under the traction-separation law (TSL) of the interface) for a wide range of cases, i.e. $G_c^E \approx G_c \approx \Omega$.

If the presence of defects at the interface is neglected and therefore, if it is assumed that only cohesive failure occurs over an interface that is fully covered with adhesive, the bumps in the load–displacement curve could be effectively attributed to a local change of the material properties of the adhesive, i.e. to a local, variable reduction of its fracture resistance. As a consequence, bumpy R-curves, in which the fracture resistance can significantly change during crack propagation, are obtained. However, the fracture resistance computed in this way is not an inherent material property of the adhesive, because it is affected by the presence, distribution and nature of defects at the interface. Therefore, as anticipated in the Introduction, this will be referred to as the apparent fracture resistance and denoted by G_c^{app}. Instead, the effective fracture resistance of the adhesive, G_c^{eff}, will be introduced by accounting for the reduced size of the interface area (due to the presence of defects).

For DCB specimens, whose width b is constant along the length of the specimen, we can introduce a coordinate x along the direction of crack propagation. To each coordinate x there corresponds a straight line orthogonal to the x axis, of length b, and on this line we can identify the portion of the line affected by some defect, in the form of either a void or interfacial failure. In this way, an effective width, denoted by b_{eff}, whose size depends on the width of the defects at any given point along the length of the DCB, so that $b_{eff} = b_{eff}(x)$, can be introduced.

Indicating with Π the total potential energy, from the derivation of Griffith's fracture propagation criterion (see e.g. [21]) it is easy to verify that it can be written in the usual way

$$\dot{a} > 0 \qquad \Longrightarrow \qquad -\frac{1}{b}\frac{\partial \Pi}{\partial a} = G_c \tag{2}$$

also when b is not constant for each value of the current crack length a. Therefore, if the constant b is replaced with the effective width b_{eff}, function of x, and assuming that the crack front is still orthogonal to the longitudinal direction of the specimen and therefore is fully defined for each value of a, then G_c can be replaced with the effective fracture resistance G_c^{eff}. If instead it is assumed that b is constant and equal to the width of the specimen, meaning that the interface defects are neglected, then G_c should be replaced with the apparent fracture resistance G_c^{app}. Therefore, by setting $x = a$, it can be written

$$-\frac{\partial \Pi}{\partial a} = G_c^{eff}(a) b_{eff}(a) = G_c^{app}(a) b. \tag{3}$$

The effective fracture resistance G_c^{eff}, by definition, should be an inherent property of the material but, as such, it can still be characterised by some scatter, both from specimen to specimen in the same test conditions, and within the interface of a single specimen. Therefore, G_c^{eff} will in general be a function of x, i.e. a.

The effective fracture resistance can be defined from Eq. (3) as

$$G_c^{eff}(a) = \frac{G_c^{app}(a)}{\zeta(a)}, \tag{4}$$

where $\zeta(a) = b_{eff}(a)/b$ is a factor with limit values 0 and 1 corresponding to no adhesive and no voids over the width, respectively. Therefore, in order to determine G_c^{eff} we need to determine the apparent fracture resistance (for which standards and well-established procedures exist, e.g. Ref. [19]) and the effective width of the adhesive (i.e. coefficient ζ). In this work, we will in particular focus on the latter.

It should be noted that $\zeta(a)$ in Eq. (4) takes into account both interfacial failure and voids. The portion of the width affected by interfacial failure, b_i must take into account interfacial failure on each of the plates, so that $b_i = b_{it} + b_{ib}$, where indices t and b refer

to the top and bottom plate, respectively. On the other hand, the portion of the width with voids will be denoted by b_v. In addition, we will assume that the fracture resistance in the case of interfacial failure, G_c^i, is smaller than that in the case of cohesive failure, G_c^{eff}. By introducing a coefficient α, this can be written as $G_c^i = \alpha\, G_c^{eff}$, with $0 < \alpha < 1$. Note that the value of coefficient α could change along the interface because the lack of adhesion that triggers interfacial failure could be caused by variable type and degree of local imperfections on the adherend's surface. However, not only is it impossible to determine the distribution $\alpha(a)$ a-priori, but it also cannot be done in an accurate manner by analysing the crack surfaces of the broken specimens, which will be discussed in more detail in Section 3.3. Therefore, for the sake of simplicity, we will assume that α is a constant. By separating the contributions of the interfacial and cohesive failure in Eq. (3), we obtain

$$G_c^{eff}(a) b_{eff}(a) = G_c^i(a) b_i(a) + G_c^{eff}(a) \left[b - b_v(a) - b_i(a)\right], \tag{5}$$

whereby it follows that

$$b_{eff}(a) = b - (1-\alpha)\left[b_{it}(a) + b_{ib}(a)\right] - b_v(a) \tag{6}$$

Therefore, in order to determine b_{eff}, we will need to measure the amount of voids and interfacial failure on each plate over the width for any position along the interface. The procedure for extracting these data from the broken specimens is proposed in the next subsection.

3.2. Defect-data extraction procedure by image processing of fracture surfaces

The proposed procedure for identifying and quantifying defects at the interface is based on the photographs of the broken specimens' crack surfaces. Interfacial failure completely removes the adhesive from one part of the specimen, leaving the aluminium surface open. When photographed under the light, this surface will shine and clearly distinguish itself from the matt surface of the adhesive where cohesive failure has occurred. Likewise, the inner surface of voids, unlike the surface of the broken adhesive where cohesive failure occurred, has a glossy finish that also shines when photographed under the light. Therefore, the same technique can be applied to identify both interfacial failure and voids.

The proposed procedure for extracting the defect data from the photographs is described by the three columns in Fig. 3 for a representative specimen. In the first column (Fig. 3(a)), the surfaces of the broken adhesive on the top and bottom plate are shown. These images have been obtained by cropping out from the original photos everything except the interface surface and then transforming this quadrilateral area to a perfect rectangle with length-to-width aspect ratio 197:25.4. The upper edge of this rectangle corresponds to the initial crack tip, whereas the lower edge corresponds to the free end of the DCB. The positions of the initial crack tip and the free end of the specimen correspond to $a_0 = 40$ mm and $a_{max} = L - b/2 = 237$ mm, respectively, while the width of the interface is $b = 25.4$ mm. Note that the value of a_{max} has been rounded to integer for the sake of simplicity, as the resulting error is only 0.13%.

The photos from Fig. 3(a) are first converted to an RGB format and then, using only the blue channel, contrast and brightness are adjusted manually. By applying binarisation, the image is converted to black and white, which is the result shown in Fig. 3(b). Black colour represents cohesive failure, while the defects (interfacial failure and voids) are depicted in white.

These photos of the top and bottom surfaces have 1973×254 black or white pixels each and, by comparing pixels at each position, four cases can be easily distinguished, namely cohesive failure, interfacial failure on the top plate, interfacial failure on the bottom plate and void. For example, by denoting black and white colour by 0 and 1, respectively, summing the photos of the top and bottom surface will give 0 in case of cohesive failure and 2 in case of voids. On the other hand, subtracting the bottom surface from the top surface will give 1 in case of interfacial failure on the top plate and -1 in case of interfacial failure on the bottom plate. By summing the result of all pixels over the width at each position along the length, $b_{it}(a)$, $b_{ib}(a)$ and b_b can be obtained. Such data contains some amount of experimental scatter, which is mostly due to variations of the photo quality (light, sharpness, resolution etc.) and imprecisions of the procedure for extracting the data, such as manual adjustment of contrast and brightness (which can alter the final black-and-white result) and overlapping (summing or subtracting) the photos of the top and bottom plate that are not perfectly aligned. All these factors are responsible for creating some artificial interfacial failure in the final result (see Fig. 3(c)), but, as it will be shown later, this is compensated by choosing a value of coefficient α that provides the best agreement with experimental load–displacement data and/or R-curves of the apparent fracture resistance. The data is finally filtered using a 9-point average, which gives results presented in Fig. 3(d). The complete procedure for extracting the defect-distribution data from raw photos is coded in *Wolfram Mathematica* and the code is available for download from the link provided in the "Supplementary data" section.

By comparing the top and the bottom surfaces in Fig. 3, it can be noticed that in the first (upper) part of the interface (for x between 40 and approximately 90 mm), interfacial failure is dominant. For the rest of the interface surface (for $x > 90$ mm), it can be noticed that the voids are mostly dominant because the white patterns are nearly symmetrical. However, because of the aforementioned imprecisions, a non-negligible amount of artificial interfacial failure is obtained around the voids.

In the next subsection we will first present a procedure for determining the apparent fracture resistance and then, using the extracted defect-distribution data, we will compute the effective fracture resistance and determine an optimal value of coefficient α.

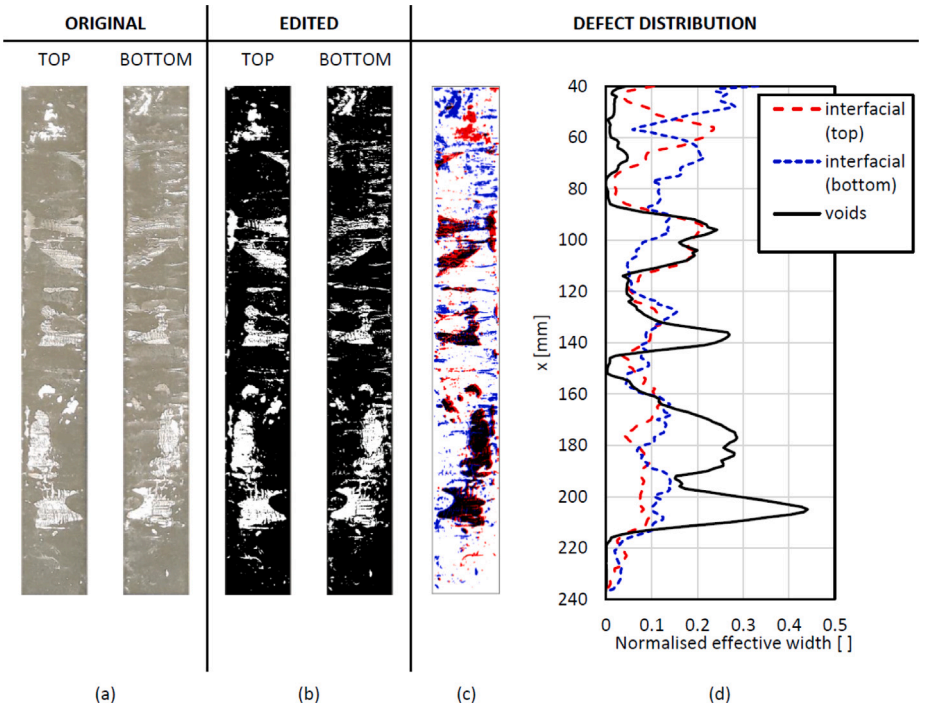

Fig. 3. Example of extraction of defect-distribution data on a representative specimen: the original (a) and the processed photos (b) of the broken adhesive surfaces for both plates, the obtained 2D defect-distribution (c) including voids (black areas) and interfacial failure on the top (red areas) and bottom surface (blue areas) and the longitudinal distribution of the defects (d).

3.3. Approximate calculation of the local values of the effective fracture resistance

In order to compute the apparent fracture resistance we will use a data-reduction scheme based on the equivalent crack length, which does not require the experimental measurement of the crack length. The equivalent crack length is the value of the crack length that, using the measured values of the applied load F and displacement υ, satisfies the simple beam deflection formula for a cantilever beam. In the case of Euler–Bernoulli beam theory, the equivalent crack length will be denoted by a_{eq}^E and is defined by the following equivalent relationships [21]:

$$\upsilon = \frac{2F(a_{eq}^E)^3}{3EI} \iff F = \frac{3EI\upsilon}{2(a_{eq}^E)^3} \iff a_{eq}^E = \sqrt[3]{\frac{3EI\upsilon}{2F}} \tag{7}$$

By doing this, we are assuming that DCB arms are clamped at an 'equivalent' crack tip, which does not correspond to the actual crack tip. In fact, because at the actual crack tip both relative separation and rotations of the arms can occur before failure, for the same values of F and υ, the equivalent crack length will be always larger than the actual one. Assuming that the equivalent crack length is a function of the actual one, i.e. $a_{eq}^E = a_{eq}^E(a)$, for a case with prescribed cross-head displacement υ, the applied load can be written as $F = F(\upsilon, a_{eq}^E(a))$. Note that function $a_{eq}^E(a)$ cannot be determined without measuring the actual crack length. Therefore, in the present work we will only assume that this functional dependency exist, but it is not known. Since

$$\Pi = \Pi(\upsilon, a) = \frac{1}{2}F\upsilon = \frac{1}{2}F(\upsilon, a_{eq}^E(a))\upsilon \tag{8}$$

using Eq. $(7)_2$ we have:

$$\frac{\partial \Pi}{\partial a} = -\frac{\upsilon}{2}\left(\frac{9EI\upsilon}{2(a_{eq}^E(a))^4}\right)\frac{\mathrm{d}a_{eq}^E}{\mathrm{d}a} \tag{9}$$

It was shown in Ref. [21] that $\mathrm{d}a_{eq}^E/\mathrm{d}a$ is extremely close to unity for a wide range of cases in a DCB test. In other words, although the difference $\Delta a^E = a - a_{eq}^E(a)$ is in general not negligible, it can be considered constant across the crack length. Therefore, replacing υ from Eq. $(7)_1$, we can write:

$$-\frac{\partial \Pi}{\partial a} \approx \frac{F^2(a_{eq}^E(a))^2}{EI} \tag{10}$$

and the equivalent crack can be approximated as

$$a_{eq}^E(a) = a + \Delta a^E \tag{11}$$

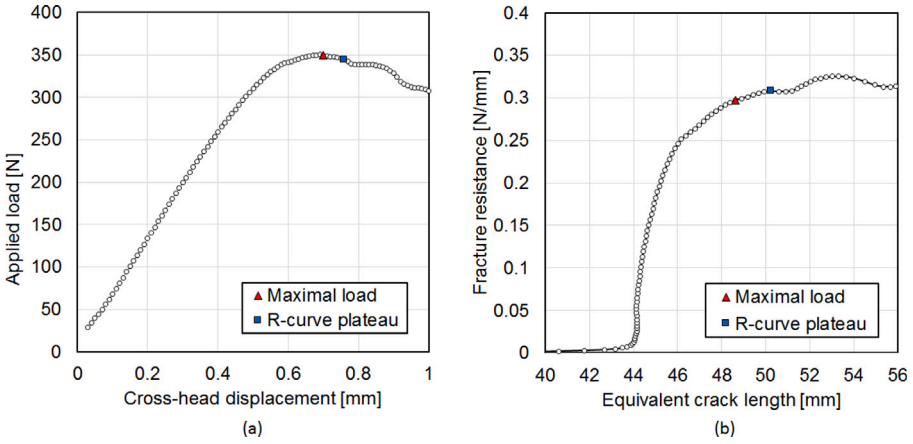

Fig. 4. Load–displacement plot (a) and the equivalent R-curve (b) for the representative specimen.

Assuming that Δa^E can be determined (or at least approximated), the effective fracture resistance can be computed as

$$G_c^{eff}(a) \approx \frac{F^2(a_{eq}^E(a))^2}{b_{eff}(a)EI} \tag{12}$$

Substituting this result in Eq. (4) gives the same result as combining Eqs. (1) and $(7)_1$, which confirms that $G_c^{app} = G_c^E$ and the apparent fracture resistance can be therefore computed as

$$G_c^{app}(a) \approx \frac{F^2(a_{eq}^E(a))^2}{b\ EI} \tag{13}$$

Plotting function (12) would give the effective R-curve, which is expected to be smoother than the apparent one, because the bumps in the load–displacement curve can be compensated by taking into account the reduced effective width of the adhesive on the interface. As Δa^E in Eq. (11) is unknown, obtaining the effective R-curve is not straightforward. However, a relatively simple method for estimating the value of Δa^E is proposed below.

Using load–displacement data of the representative specimen, produced for each increment of displacement $\Delta v = 0.01$ mm, the equivalent crack length a_{eq}^E and the corresponding value of G_c^E have been computed for each available pair (F, v) using Eqs. (7) and (1), respectively. The first part of the load–displacement plot and the equivalent apparent R-curve (G_c^E-a_{eq}^E plot) are given in Fig. 4. Note that G_c^E represents the apparent fracture resistance only when the crack is propagating, i.e. when $\dot{a} > 0$. However, because the experimental crack-length measurements are not available, determining whether the crack propagates or not has to be done in an indirect way.

Virtual experiments with perfect interface (such as those performed in [21]) show that crack propagation will start when a plateau of the equivalent apparent R-curve plotted for all available (F, v) pairs is reached. Before that, G_c^E computed for (F, v) pairs with $\dot{a} = 0$ will increase very rapidly and obviously does not represent the apparent fracture resistance. Because in Fig. 4(b) the plateau of the apparent R-curve is not a straight line (due to defects on the interface), the start of crack propagation has been assumed at the point with the smallest value of a_{eq}^E where the incremental change of G_c^E with respect to a_{eq}^E changes sign (i.e. $\mathrm{d}G_c^E/\mathrm{d}a_{eq}^E \approx 0$). Note that the cross-head displacement of that point is larger than that corresponding to F_{max}, which is shown in Fig. 4(a). This is due to the development of the damage-process zone in front of the crack tip before crack propagation [22].

Thus, for the representative specimen, the first point on R-curve plateau corresponds to $a_{eq}^E(a_0) = 50.24$ mm, which from Eq. (11) gives $\Delta a^E = 10.24$ mm. Note that Δa^E is not the length of the damage-process zone (DPZ) because in the concept of equivalent crack length, besides damage softening, linear elastic behaviour (which also results in relative displacement and rotations of DCB arms at the crack tip) is neglected in front of the crack tip. Therefore, the DPZ should be certainly shorter than Δa^E.

Using this result it is possible to compute the apparent and the effective R-curve with approximated crack length a on the horizontal axis. In Fig. 5, a comparison between the normalised apparent R-curve and the distribution of the normalised effective width of the adhesive, $\zeta(a)$ along the interface is shown for the entire range of possible values of coefficient α between its limits 0 and 1. It can be noticed that the extracted defect data resembles the shape of the normalised apparent R-curve fairly well, but it is strongly influenced by the value of α.

The values of the fracture resistance are normalised with respect to the maximum value of G_c^E, $\max(G_c^E)$, computed during crack propagation. For the representative specimen $\max(G_c^E) = 0.352$ N/mm was obtained for $a \approx 217$ mm. By doing so we are assuming that at that location there are no defects at the interface. In fact, as it can be seen in Fig. 5, the effective adhesive width at that location reaches its maximal value (very close to 100%). Values of $G_c^E(a)$ used in Fig. 5 have been computed for the same values of a as the defect-distribution data $\zeta(a)$ by linear interpolation of the closest values computed for the fixed values of the prescribed displacement v. Note also that the last value of G_c^E used in the same plot corresponds to $a = 220$ mm, which is due to the abrupt separation of the plates when the crack approaches the right-hand end of the specimen.

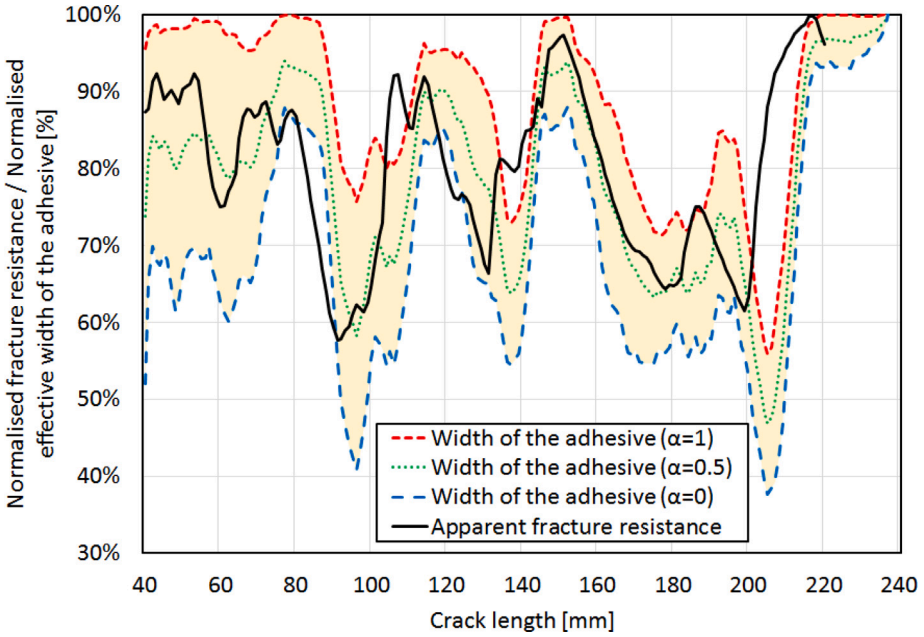

Fig. 5. Distribution of the normalised apparent fracture resistance ($G_c^E(a)/\max(G_c^E)$) and the mean defect-distribution data ($\zeta_m(a) = b_{eff}(a)/b$) along the interface, with the latter additionally filtered using a 9-point average, for the representative specimen.

Table 2
Average values (AVG), standard deviation (SD) and coefficient of variation (CV) for the normalised effective width of the adhesive ζ, normalised apparent fracture resistance G_c^{app} (computed as $G_c^{app}(a) = G_c^E(a)/\max(G_c^E)$) and normalised effective fracture resistance (computed as $G_c^{eff}(a) = G_c^{app}(a)/\zeta(a)$) for different values of coefficient α.

Function of a		AVG	SD	CV
normalised G_c^{app}		80.14%	11.13%	13.89%
$\alpha = 0$	ζ	69.09%	15.01%	21.73%
	normalised G_c^{eff}	123.74%	25.82%	20.87%
$\alpha = 0.5$	ζ	78.92%	12.55%	15.90%
	normalised G_c^{eff}	105.46%	18.77%	17.80%
$\alpha = 1$	ζ	88.75%	11.20%	12.62%
	normalised G_c^{eff}	92.40%	15.49%	16.76%

It can be noticed from Fig. 5 that, at some locations, no value of coefficient α can capture the shape of the normalised apparent R-curve. This indicates that either the void-extraction procedure is not sufficiently accurate or there are effects other than defects in the adhesive layer that can alter fracture resistance of the adhesive. It is expected that, by employing a more reliable method for obtaining the defect-distribution data, such as 3D [2,23] or X-ray [6] scans, an even better correlation between $\zeta(a)$ and normalised $G_c^{app}(a)$ would be obtained.

The normalised effective fracture resistance could be computed by dividing the normalised apparent fracture resistance by $\zeta(a)$ (both plotted in Fig. 5). However, this is not done here because these two plots are still not close enough, which does not reduce, but instead amplifies the fluctuations in the normalised effective R-curve.

Instead of adding the normalised effective R-curve to Fig. 5, which would make the figure less clear, the results are given in Table 2. It can be noticed that, independently from the value of α, the coefficient of variation (CV) for the normalised effective fracture resistance is higher than for the normalised apparent fracture resistance, which, considering our hypothesis that G_c^{eff} (unlike G_c^{app}) is an inherent material property, cannot be an acceptable result. It is obvious that a representative effective R-curve ($G_c^{eff}(a)$) cannot be obtained in this way due to all inaccuracies mentioned earlier. Moreover, for $\alpha = 1$, the average of $G_c^{eff}(a)$ is less than $\max(G_c^{app}(a))$, which should not be the case if we assume that the average value of G_c^{eff} (as an inherent material property) is representative for the entire interface.

Therefore, b_{eff} cannot be obtained without making any a-priori assumptions on the relationship between G_c^{app} and G_c^{eff}, and/or the value of coefficient α. As for the latter, from now on we will assume that $\alpha = 0.5$ because the results of Fig. 5 show that this assumption is reasonable and sufficiently accurate. Moreover, as it will be shown in Section 3.4, introducing this assumption will significantly simplify the expression for b_{eff}. Also, because we previously concluded that the effective R-curve cannot be

accurately determined using the available data, we will now focus our attention on obtaining the average value of G_c^{eff} that will be representative for the entire interface or, more generally, for a specific type of adhesive.

3.4. Calculation of a weighted average of the effective fracture resistance

Assuming that $\alpha = 0.5$, Eq. (6) can be rewritten as

$$b_{eff}(a) = b - \frac{b_{dt}(a) + b_{db}(a)}{2}, \tag{14}$$

where for a given a, $b_{dt} = b_v + b_{it}$ and $b_{db} = b_v + b_{ib}$ represent the total amount of defects (voids and interfacial failure) on the top and bottom plate, respectively. The amount of adhesive on each plate can be then defined as

$$\zeta_t(a) = \frac{b - b_{dt}(a)}{b} \quad \text{and} \quad \zeta_b(a) = \frac{b - b_{db}(a)}{b}, \tag{15}$$

for the top and bottom plate, respectively. Thus, Eq. (14) finally becomes

$$b_{eff}(a) = \frac{\zeta_t(a) + \zeta_b(a)}{2} b = \zeta_m(a) b, \tag{16}$$

where $\zeta_m(a)$ is the distribution of the mean amount of adhesive on both plates at position a. Note that in our defect-data extraction procedure $\zeta_t(a)$ and $\zeta_b(a)$ correspond to the amount of white pixels (see Fig. 3(b)) on the top and bottom plate, respectively, which makes them easy to obtain, but as such, they contain no information about the type of the defect (void or interfacial failure). However, obtaining the effective adhesive width from Eq. (16) without this information is possible only because we previously assumed that $\alpha = 0.5$.

Taking the average of both sides of Eq. (4) over the entire specimen gives

$$\hat{G}_c^{eff} = \frac{1}{\overline{\zeta}_m} \bar{G}_c^{app} \tag{17}$$

where

$$\hat{G}_c^{eff} = \frac{1}{\int_{a_0}^{a_{max}} \zeta_m(a) da} \int_{a_0}^{a_{max}} G_c^{eff}(a) \zeta_m(a) da \tag{18}$$

is the weighted average of G_c^{eff},

$$\overline{\zeta}_m = \frac{1}{a_{max} - a_0} \int_{a_0}^{a_{max}} \zeta_m(a) da \tag{19}$$

is the average value of ζ_m,

$$\bar{G}_c^{app} = \frac{1}{a_{max} - a_0} \int_{a_0}^{a_{max}} G_c^{app}(a) da \tag{20}$$

is the average of G_c^{app} and a_{max} is the maximal value of the crack length for which experimental (F, v) data is available. Note that usually a_{max} does not reach to the end of the specimen ($a_{max} < L - b/2$) because the last part of the crack propagation is unstable due to final dynamic collapse.

As G_c^{app} are ζ_m are not true functions in the practical implementation of the procedure, but lists of values computed at discrete points (co-ordinates x), their averages can be approximated as

$$\bar{G}_c^{app} \approx \frac{1}{n+1} \sum_{i=0}^{n} G_{c.i}^{app} \tag{21}$$

$$\overline{\zeta}_m \approx \frac{1}{n+1} \sum_{i=0}^{n} \zeta_{m.i} \tag{22}$$

where $G_{c.i}^{app}$ and $\zeta_{m.i}$ are the apparent fracture resistance and mean defect distribution determined at point i ($i = 0, 1, 2, \ldots, n$) that corresponds to position $a = a_0 + i$ in mm (because in our case adjacent points are 1 mm apart). Although through image-processing $\zeta_{m.i}$ can obtained for the entire interface (i.e. $n = 197$), as explained earlier, the number of points n for which $G_{c.i}^{app}$ can be computed will typically be less than 197 because of the final dynamic collapse. This small discrepancy will be here neglected and, for the sake of simplicity, different values of n will be used in Eqs. (21) and (22). Our preliminary analyses have shown that this simplification has a negligible influence on the final values of $\overline{\zeta}_m$.

For the representative specimen, $\overline{\zeta}_m = 0.79$ obtained from Eq. (22) with $n = 197$ gives the average effective adhesive width $\overline{b}_{eff} = 20.06$ mm. This means that for this specimen, 21% of the interface has defects. From (21) it follows that $\bar{G}_c^{app} = 0.282$ N/mm, with $n = 180$. It should be emphasised that in order to obtain this result, the actual crack length a has been estimated using the approach presented in the previous subsection for each measured (F, v) pair. For the same dataset, the apparent fracture resistance has been computed using the formula for G_c^E (Eq. (1)). Then, using linear interpolation, values of $G_{c.i}^{app}$ have been computed for values of the actual crack length $a = a_0 + i$, where $i = 0, 1, 2, \ldots, 180$. Finally, the average value of the effective fracture resistance follows from (17) as $\hat{G}_c^{eff} = 0.357$ N/mm. Note that this value is within 1.5% of the maximum computed value of the apparent fracture resistance $\max(G_c^E) = 0.352$ N/mm.

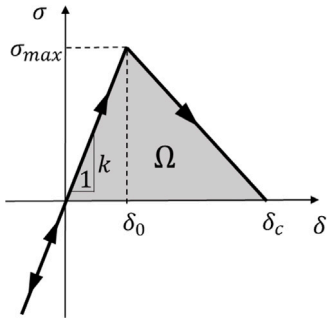

Fig. 6. Bi-linear traction-separation law (TSL) embedded in the CZM.

Although this procedure for obtaining $\hat{G}_c^{eff}$ is relatively simple, it could be simplified even more by avoiding the estimation of the actual crack length and compute the average of the apparent fracture resistance not with respect to the crack length a (or coordinate x), but with respect to the cross-head displacement v (as the experiments were displacement-controlled). Therefore, for the sake of simplicity, $\bar{G}_c^{app}$ can be computed as the average of all values of G_c^{app} computed from (1) for each $v-F$ pair after the peak load, i.e. during crack propagation.

By taking the average of all values of G_c^{app} computed from (1) during crack propagation for an increment of the cross-head displacement $\Delta v = 0.01$ mm, $\bar{G}_c^{app} = 0.285$ N/mm has been obtained, which is only approximately 1% higher than the value obtained from (21). Thus, the procedure for computing $\bar{G}_c^{app}$ can be simplified without significantly affecting the accuracy.

In order to account for shear deformability of the DCB arms, instead of using Eq. (1), G_c^{app} can be computed using the Enhanced-Simple-Beam-Theory (ESBT) data-reduction scheme [24] as

$$G_c^{app} \approx \frac{F^2}{b}\left(\frac{a_{eq}^2}{EI} + \frac{1+2a_{eq}\sqrt{\alpha^*}}{\mu A_s}\right) \tag{23}$$

where μA_s is the shear stiffness of DCB arms computed as the product of the shear modulus μ, cross-sectional area A and the shear-correction coefficient $k_s = 5/6$, $\alpha^* = \mu A_s / EI$, while the equivalent crack length is defined as

$$a_{eq} = \sqrt[3]{\left(\frac{1}{\sqrt{\alpha^*}}\right)^3 + (a_{eq}^E)^3} - \frac{1}{\sqrt{\alpha^*}}, \tag{24}$$

with a_{eq}^E defined in (7). For the representative specimen, values of G_c^{app} computed using Eqs. (1) and (23) are essentially the same. This is in line with the results presented in Ref. [24], where it was confirmed that taking into account shear strains has a very small effect on the computed fracture resistance using the concept of equivalent crack length, even for arms that are more shear-deformable than the aluminium ones used in the present work (e.g. arms made of composite materials). For an even more sophisticated definition of the equivalent crack length see Ref. [25].

In the next section we will use $\hat{G}_c^{eff}$ and $\zeta_m(a)$ as an input for numerical simulations, whose results will illustrate the influence of the defects on the interface on the load–displacement response of the DCB. In addition, in Section 4.2, the numerical model will be used to demonstrate that in general $G_c^{eff} \neq G_c^{app}/\zeta$ along the interface.

4. Numerical simulations

4.1. Numerical model with a variable adhesive width

The concepts of apparent and effective fracture resistance can be relatively easily implemented in numerical modelling of debonding. In this work, we use the finite-element model for DCB tests presented by the authors in Ref. [13], where relevant details can be found. Note that the model used in the present work is rate-independent [26,27], which is a simplification of the rate-dependent model implemented in [13]. We will now briefly review the cohesive-zone model (CZM), based on the bi-linear traction-separation law (TSL), focussing on the changes needed to take into account a variable width.

In a bi-linear TSL, depicted in Fig. 6(a), besides the fracture resistance, here denoted by Ω and representing the work of separation (the area under the TSL), two additional parameters, namely the maximal normal traction σ_{max} and the initial stiffness k, are required. As shown in Ref. [21] and discussed earlier, it will be assumed that $\Omega \approx G_c$. It was also demonstrated in [13] that the three parameters of the bi-linear CZM can be instantaneously and accurately identified using the free software *DCB PAR* [28]. Because in this approach a fully bonded interface is assumed, these are actually the apparent interface parameters.

While the influence of the width of the adhesive on the value of the fracture resistance follows directly from the definition of G_c, its influence of other parameters of the bi-linear CZM is less obvious. However, analytical expressions derived in [22] and used in the parameter-identification algorithm presented in [28] clearly confirm that, for the same load–displacement data, reducing the

Table 3
Apparent and effective values of parameters defining the bi-linear TSL for the case of the representative specimen. The apparent parameters were identified using *DCB PAR* software [28].

Parameter	Apparent	Effective
Ω [N/mm]	0.285	0.361
σ_{max} [N/mm^2]	39.66	50.20
k [N/mm^3]	73 340	92 835

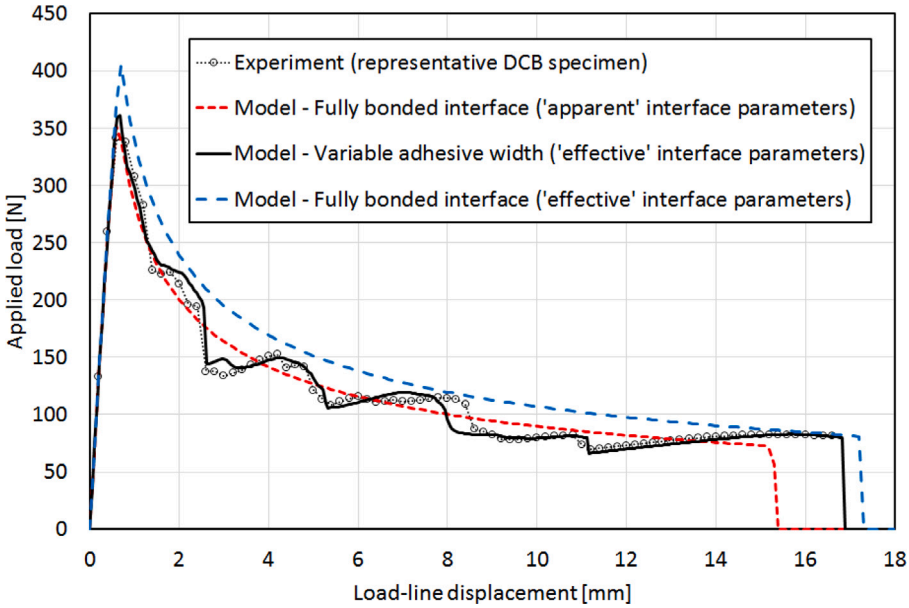

Fig. 7. A comparison between the results of DCB-test simulations using the apparent and effective interface parameters, and the experimental results for the representative specimen.

width of the interface by a factor $\overline{\zeta}_m$ (where $\overline{\zeta}_m < 1$), increases the values of σ_{max} and k by a factor $1/\overline{\zeta}_m$. From there, it can be easily shown that by reducing the width of the adhesive, characteristic values of the relative displacements δ_c and δ_0 (see Fig. 6(a)) remain unchanged.

Therefore, the effective values of Ω, σ_{max} and k for the case of interface with defects can be obtained by dividing the apparent parameters by $\overline{\zeta}_m$. In Table 3, a comparison between the apparent and the effective parameters is given for the representative specimen with $\overline{\zeta}_m = 0.79$. Note that *DCB PAR* [28] computes $\tilde{G}_c^{app}$ not according to (21), but using values of G_c^{app} computed for equidistant cross-head displacements during crack propagation, as explained at the end of Section 3.4.

As for the displacement input parameters, *DCB PAR* provides values of $\delta_0 = 5.41 \cdot 10^{-4}$ mm and $\delta_c = 0.014$ mm, which are both apparent and effective parameters, as previously noted.

Once the effective interface parameters are known, the next step is to use the complete mean defect-distribution data $\zeta_m(a)$ as the input for the numerical model. Contributions of the interface to the residual vector and stiffness matrix (see [13] for complete expressions) are computed by taking into account the variation of the effective width of the adhesive along the interface. In each integration point in each finite element, the effective width of the interface is computed from the available $\zeta_m(a)$ data by linear interpolation.

Three different simulations have been performed, whose results are given in Fig. 7 for the representative specimen. In the first simulation (dashed red line), a fully bonded interface is assumed and the apparent values of the interface parameters used. This is also the commonly used approach. In the second simulation (solid black line), the variable effective width of the adhesive along the interface is modelled using the defect-distribution data $\zeta_m(a)$ and the effective interface parameters. Finally, a 'fully bonded' interface (the width is not scaled) with the effective interface parameters is modelled in the third simulation (dashed blue line).

It can be noticed that the model with variable adhesive width and the effective interface parameters (solid black line) can capture the bumps in the experimental load–displacement data with a good level of accuracy. This result confirms that the bumps in load–displacement plots DCB tests can be attributed principally to the defects of the interface. The model also accurately captures the final failure of the DCB specimen, which is not the case when the apparent interface parameters are used and fully bonded interface assumed (dashed red curve).

It is important to note that results shown in Fig. 7 have been obtained without any manual curve fitting as they follow directly from strictly defined crack-surface photo analyses and parameter-identification procedures.

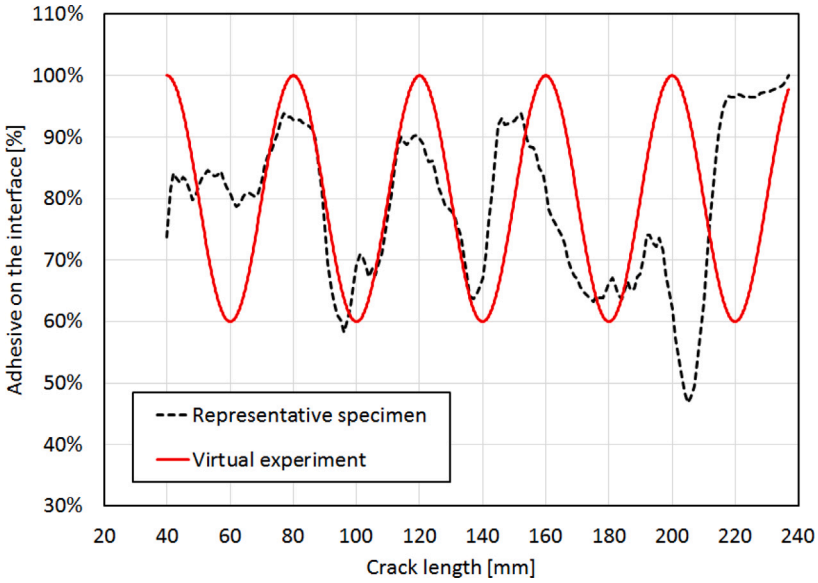

Fig. 8. Mean defect distribution ζ_m from the representative specimen and the one assumed in the virtual experiment.

4.2. Virtual experiment on a specimen with variable width of adhesive layer

It was noted in Section 3.3 that, in Fig. 5, a perfect correlation between the normalised apparent fracture resistance and the mean defect-distribution data ζ_m is not expected for a number of reasons. A very small discrepancy can be expected due to the assumption that $\Delta a^E = a - a^E_{eq}(a)$ is constant, which is nearly but not strictly true. Another reason for expecting some discrepancy is that the 2D defect-distribution data is lumped on a 1D function ζ_m, in which the actual 2D distribution of defects and the distinction between voids and interfacial failure are both averaged out. Furthermore, even if we wanted to employ the full data on the 2D distribution of defects and on their nature, the 1D beam model used would not capture its effects.

On the other hand, if all potential sources of error were excluded, there would still be another reason for the above-mentioned discrepancy in Fig. 5. This is investigated in this section, by analysing some suitably constructed 'virtual experiments'. More precisely, using a numerical model in which a variable width of the adhesive layer along the interface is given as an input, the relationship between the apparent and effective fracture resistance defined in Eq. (4) will be investigated. Simulations have been conducted using the same finite-element model used for the simulations reported in Section 4.

Defect distribution data reported in Fig. 5 is here replaced by a sinusoidal function for $\zeta_m(a)$ that oscillates around the mean value $\overline{\zeta}_m = 0.8$ with an amplitude of ±20% and wavelength of 40 mm (see Fig. 8). Such a regular distribution, instead of the actual one, is used to show how same defects can cause different behaviour depending on their location along the interface.

For the virtual experiment, the value $\Omega = 0.35$ N/mm was chosen because it corresponds to the maximum value of the apparent fracture resistance computed for the representative specimen, which is also expected to be close to its effective fracture resistance. The peak interface traction and stiffness of the linear-elastic part were assumed to be $\sigma_{max} = 50$ N/mm^2 and $k = 9000$ N/mm^3, respectively. By keeping the same values of Ω and k while increasing σ_{max}, the behaviour of the adhesive becomes more brittle.

Using the same geometrical and material data for the DCB arms as those reported in Section 2, the load–displacement curve shown in Fig. 9 has been obtained. Not only does it confirm that defects on the interface cause bumps in the force–displacement plots obtained in DCB experiments, but it shows also shows that the same pattern of defects can lead to unstable crack propagation depending on its location at the interface. Such behaviour is represented by snap-backs in the load–displacement plot that have been captured using the damage-based arc-length method [29]. Obviously, in a real displacement-controlled experiment, such snap-backs would be cropped and substituted with a (nearly) vertical line, which can be seen also in Fig. 7. The last and the largest snap-back in Fig. 9 corresponds to the final detachment of the plates. It can be noticed that the load–displacement curve for the interface with sinusoidal defect distribution oscillates between curves obtained for the limit cases with no defects and constant 40% voids, that correspond to limits (extremes) of the void distribution given in Fig. 8.

It is noticed that the longer the crack, the less stable the crack propagation. In fact, sharper snap-backs can be observed for larger crack lengths. This can be explained by the fact that all repetitive drops in the load–displacement curve must have the same area because the same defect-distribution patterns shown in Fig. 8 are repeated periodically. The shape of these drops in a load–displacement plot changes because the amount of crack propagation per unit increment of cross-head displacement reduces as the crack advances. This explains why in order to compensate the energetic drop due to voids, besides reducing the force, for longer cracks it is also necessary to reduce the displacement, which leads to snap-backs.

Incidentally, the transition from snap throughs to snap backs, as well as the increased steepness of the latter with further increase in crack propagation, may also explain the fact that, when oscillations of the load–displacement curves are due to a not sufficiently

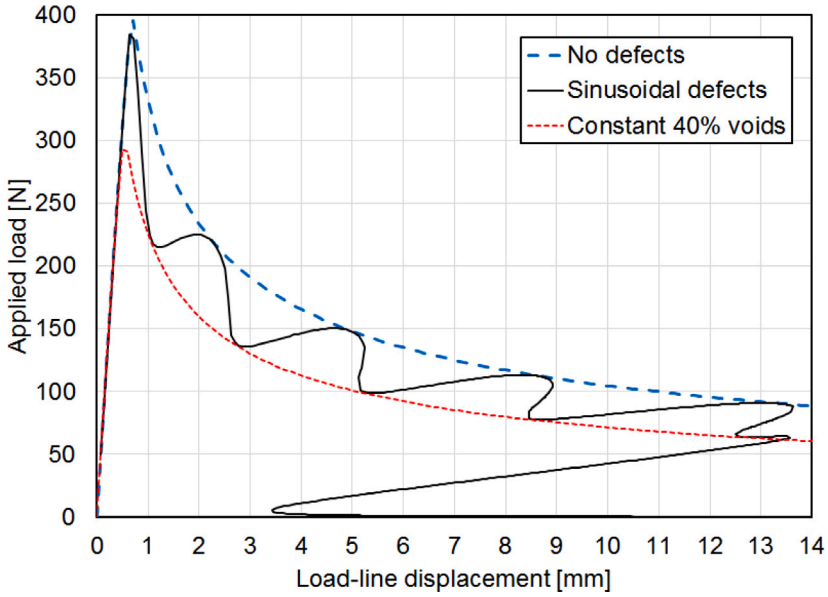

Fig. 9. Force–displacement plot obtained using the damage-based arc-length method [29] for the sinusoidal defect distribution over the interface given in Fig. 8. In addition, the force–displacement curves for interface without defects and constant 40% voids are given.

refined mesh across the cohesive zone in a numerical model, convergence of an incremental implicit nonlinear solution procedure becomes more and more difficult as the crack propagates, even when arc length procedures are used [26,30].

The R-curve of the apparent fracture resistance computed using formula (1) for G_c^E has been normalised with respect to Ω and shown in Fig. 10. It can be noticed that the normalised R-curve resembles the sinusoidal shape of ζ_m, but is shifted to the left with respect to it. Additional analyses, not shown here for the sake of brevity, confirmed that this shift reduces as the adhesive becomes more brittle, i.e. with increasing σ_{max}, while keeping Ω and k unchanged. This suggests that for $\sigma_{max} \to \infty$ the apparent R-curve and the plot of ζ_m would overlap. In other words, based on these virtual experiments we can conclude that definition (4) of the effective fracture resistance is strictly valid only for the LEFM limit case. Obviously, the more brittle the adhesive, the more accurate the prediction of the effective fracture resistance using formula (4). Moreover, reducing σ_{max} increases the length of the DPZ and in turn makes the crack propagation more stable and less sensitive to the presence of defects. In fact, as reported in [10,11], the size of the DPZ will determine the sensitivity of the load–displacement response to the presence of voids and in turn the stability of the crack propagation.

It can be concluded that the computed values of G_c^{app} are influenced not only by the local values of ζ_m, but also by values of ζ_m in front of the crack tip, i.e. inside the DPZ. The smaller the DPZ, the shorter the anticipation (i.e. the horizontal shift). Results shown in Fig. 10 confirm that the distribution of defects along the interface (i.e. ζ_m) transfers to the R-curve.

Based on these observations it can be concluded that obtaining the effective fracture resistance cannot be done accurately using expression (4) even using perfectly accurate data from virtual experiments, in which all the issues mentioned at the start of this section do not arise.

5. Conclusions

In this work, the influence of imperfections in the adhesive layer (consisting of voids and interfacial failure) on the fracture resistance of adhesive joints in mode-I debonding has been studied, which led to the following conclusions:

- A relationship between the effective fracture resistance, computed by taking into account a reduced effective width of the adhesive layer due to defects, and the apparent fracture resistance, obtained by neglecting any imperfections at the interface, is presented. It has been shown that bumpy R-curves of the apparent fracture resistance clearly resemble the plot of the effective adhesive width over the interface.
- A novel procedure based on image processing of the photographs of the cracked surfaces of DCB specimens has been proposed for extracting the defect-distribution data (both voids in the adhesive layer and interfacial failure). The procedure has proven to be relatively easy to implement and capable of identifying the distribution of imperfections over the interface with satisfactory accuracy.
- By means of virtual experiments, in which defect-distribution data and effective interface parameters are known in advance, it has been shown that the apparent R-curve anticipates the plot of the defect-distribution data by a value that depends on the brittleness of the adhesive, i.e. the size of the damage-process zone.

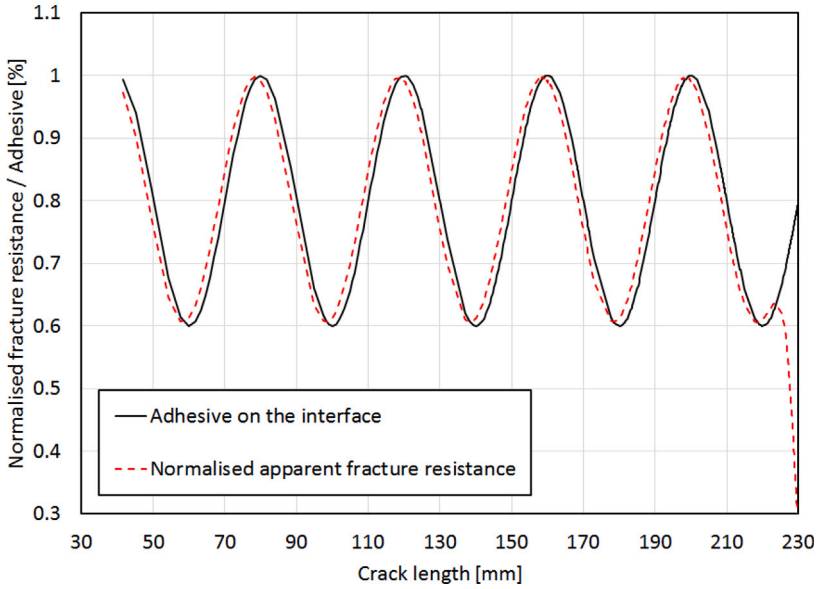

Fig. 10. Normalised R-curve of the apparent fracture resistance compared to the effective width of the adhesive on the interface.

- A simplified approach for identifying the effective interface parameters for the purpose of numerical modelling, in which the average value of the effective fracture resistance is computed by dividing the average values of the apparent fracture resistance by the average value of the defect-distribution data over the interface, has been presented. Using the average effective interface parameters and the identified defect-distribution data in the numerical model, good agreement between the results of simulations and the experimental load–displacement curves have been obtained. Moreover, the proposed procedures for obtaining the defect-distribution data and apparent interface parameters are essentially automatic, which makes them very fast and practical.

The proposed approach could be improved by introducing more sophisticated and accurate methods for detecting the imperfections at the interface, such as 3D scan or X-ray tomography. While the effect of voids can be implemented relatively easily in numerical models by reducing the interface area, assessing the fracture resistance of the areas characterised by interfacial failure requires more investigation.

CRediT authorship contribution statement

Leo Škec: Writing – review & editing, Writing – original draft, Visualization, Validation, Software, Resources, Project administration, Methodology, Investigation, Funding acquisition, Formal analysis, Data curation, Conceptualization. **Giulio Alfano:** Writing – review & editing, Writing – original draft, Validation, Resources, Project administration, Methodology, Investigation, Funding acquisition, Formal analysis, Conceptualization.

Declaration of competing interest

The authors declare the following financial interests/personal relationships which may be considered as potential competing interests: Giulio Alfano reports financial support was provided by European Union.

Acknowledgements

This research is part of the project MOLAY-STRUDEL, funded from the European Union's Horizon 2020 research and innovation programme under the Marie Sklodowska-Curie grant agreement N. 701032.

Appendix A. Supplementary data

The data underpinning this publication can be accessed from Brunel University London's data repository, Brunelfigshare here under a CCBY licence: https://doi.org/10.17633/rd.brunel.25444726.

References

[1] Bascom WD, Cottington RL. Air entrapment in the use of structural adhesive films. J Adhes 1972;4(3):193–209.
[2] Sun F, Pruncu CI, Penchev P, Jiang J, Dimov S, Blackman BR. Influence of surface micropatterns on the mode I fracture toughness of adhesively bonded joints. Int J Adhes Adhes 2020;103:102718.
[3] Chester RJ, Roberts JD. Void minimization in adhesive joints. Int J Adhes Adhes 1989;9(3):129–38.
[4] Pearce PJ, Arnott DR, Camilleri A, Kindermann MR, Mathys GI, Wilson AR. Cause and effect of void formation during vacuum bag curing of epoxy film adhesives. J Adhes Sci Technol 1998;12(6):567–84.
[5] Niklaus F, Enoksson P, Kalvesten E, Stemme G. Void-free full wafer adhesive bonding. In: Proceedings of the IEEE micro electro mechanical systems. IEEE; 2000, p. 247–52.
[6] Lißner M, Alabort E, Cui H, Rito R, Blackman BR, Petrinic N. Experimental characterisation and numerical modelling of the influence of bondline thickness, loading rate, and deformation mode on the response of ductile adhesive interfaces. J Mech Phys Solids 2019;130:349–69.
[7] Smith KR. Correlating fracture toughness and surface roughness for a ductile epoxy adhered to aluminum substrates (Master's thesis), University of Tennessee; 2021.
[8] Cuminatto C, Parry G, Braccini M. A model for patterned interfaces debonding – application to adhesion tests. Int J Solids Struct 2015;75–76:122–33.
[9] Pascuzzo A, Yudhanto A, Alfano M, Lubineau G. On the effect of interfacial patterns on energy dissipation in plastically deforming adhesive bonded ductile sheets. Int J Solids Struct 2020;198:31–40.
[10] Heide-Jørgensen S, Budzik MK. Crack growth along heterogeneous interface during the DCB experiment. Int J Solids Struct 2017;120:278–91.
[11] Heide-Jørgensen S, Budzik MK. Effects of bondline discontinuity during growth of interface cracks including stability and kinetic considerations. J Mech Phys Solids 2018;117:1–21.
[12] Budzik MK, Heide-Jørgensen S, Aghababaei R. Fracture mechanics analysis of delamination along width-varying interfaces. Composites B 2021;215:108793.
[13] Škec L, Alfano G. Experimental and numerical study of rate-dependent mode-I failure of a structural adhesive. J Adhes 2023;98(8):1323–55.
[14] Monteiro J, Campilho RDSG, Marques EAS, da Silva L. Experimental estimation of the mechanical and fracture properties of a new epoxy adhesive. Appl Adhesion Sci 2015;3:25.
[15] Sekiguchi Y, Katano M, Sato C. Experimental study of the mode I adhesive fracture energy in DCB specimens bonded with a polyurethane adhesive. J Adhes 2017;93(3):235–55.
[16] Yahya N. Failure analysis of bonded steel/CFRP laminate connections [Ph.D. thesis], University of Glasgow; 2015, PhD thesis.
[17] Álvarez D, Blackman B, Guild F, Kinlock A. Mode I fracture in adhesively-bonded joints: A mesh-size independent modelling approach using cohesive elements. Eng Fract Mech 2014;115:73–95.
[18] Blackman BR, Kinloch AJ, Rodriguez-Sanchez FS, Teo WS. The fracture behaviour of adhesively-bonded composite joints: Effects of rate of test and mode of loading. Int J Solids Struct 2012;49(13):1434–52.
[19] British Standards Institution. BS ISO 25217:2009 Adhesives - Determination of the mode I adhesive fracture energy of structural adhesive joints using double cantilever beam and tapered double cantilever beam specimens. Standard, 2009.
[20] Huntsman Advanced Materials Inc. Araldite®2015 Adhesive - Technical Datasheet. 2015.
[21] Škec L, Alfano G, Jelenić G. On G_c, J_c and the characterisation of the mode-I fracture resistance in delamination or adhesive debonding. Int J Solids Struct 2018;144–145:100–22.
[22] Škec L, Alfano G, Jelenić G. Complete analytical solutions for double cantilever beam specimens with bi-linear quasi-brittle and brittle interfaces. Int J Fract 2019.
[23] Azari S, Papini M, Spelt JK. Effect of surface roughness on the performance of adhesive joints under static and cyclic loading. J Adhes 2010;86(7):742–64.
[24] Škec L, Alfano G, Jelenić G. Enhanced simple beam theory for characterising mode-I fracture resistance via a double cantilever beam test. Composites B 2019;167.
[25] Arrese A, Boyano A, De Gracia J, Mujika F. A novel procedure to determine the cohesive law in DCB tests. Compos Sci Technol 2017;152:76–84.
[26] Alfano G, Crisfield M. Finite element interface models for the delamination analysis of laminated composites: Mechanical and computational issues. Internat J Numer Methods Engrg 2001;50(7):1701–36.
[27] Škec L, Jelenić G, Lustig N. Mixed-mode delamination in 2D layered beam finite elements. Internat J Numer Methods Engrg 2015;104(8):767–88.
[28] Škec L. Identification of parameters of a bi-linear cohesive-zone model using analytical solutions for mode-I delamination. Eng Fract Mech 2019;214:558–77.
[29] Škec L, Jelenić G. Geometrically non-linear multi-layer beam with interconnection allowing for mixed-mode delamination. Eng Fract Mech 2017;169:1–17.
[30] Alfano G, Crisfield MA. Solution strategies for the delamination analysis based on a combination of local-control arc-length and line searches. Internat J Numer Methods Engrg 2003;58:999–1048.